Band Diagram and Rate Analysis of Thin Film Spinel $LiMn_2O_4$ Formed by Electrochemical Conversion of ALD-Grown MnO

*Matthias J. Young, Hans-Dieter Schnabel, Aaron M. Holder, Steven M. George, and Charles B. Musgrave**

Nanoscale spinel lithium manganese oxide is of interest as a high-rate cathode material for advanced battery technologies among other electrochemical applications. In this work, the synthesis of ultrathin films of spinel lithium manganese oxide ($LiMn_2O_4$) between 20 and 200 nm in thickness by room-temperature electrochemical conversion of MnO grown by atomic layer deposition (ALD) is demonstrated. The charge storage properties of $LiMn_2O_4$ thin films in electrolytes containing Li^+, Na^+, K^+, and Mg^{2+} are investigated. A unified electrochemical band-diagram (UEB) analysis of $LiMn_2O_4$ informed by screened hybrid density functional theory calculations is also employed to expand on existing understanding of the underpinnings of charge storage and stability in $LiMn_2O_4$. It is shown that the incorporation of Li^+ or other cations into the host manganese dioxide spinel structure (λ-MnO_2) stabilizes electronic states from the conduction band which align with the known redox potentials of $LiMn_2O_4$. Furthermore, the cyclic voltammetry experiments demonstrate that up to 30% of the capacity of $LiMn_2O_4$ arises from bulk electronic charge-switching which does not require compensating cation mass transport. The hybrid ALD-electrochemical synthesis, UEB analysis, and unique charge storage mechanism described here provide a fundamental framework to guide the development of future nanoscale electrode materials for ion-incorporation charge storage.

1. Introduction

Spinel lithium manganese oxide ($LiMn_2O_4$) is an important material for many electrochemical applications. While $LiMn_2O_4$ is most commonly known as a high-rate cathode material for lithium ion batteries,[1] it has also been used in selective extraction of lithium from brine,[2,3] and as a cathode material in aqueous sodium sulfate for environmentally friendly, safe, and inexpensive batteries.[4] For each of these applications, cations (e.g., Li^+) are known to reversibly incorporate into the spinel manganese dioxide (λ-MnO_2) host structure during cycling.

The electrochemical lithium intercalation processes in $LiMn_2O_4$ are well-studied, having been evaluated using in situ synchrotron techniques, in situ electrochemical quartz-crystal microbalance (EQCM) experiments, and various computational and experimental approaches.[5–7] The amount of lithium present in the MnO_2 electrode, represented by x in $Li_xMn_2O_4$, is known to vary between 0.27 and 1.0 when cycled over a potential range of 3.8–4.2 V versus Li^+/Li.[5] Within this potential range, two equilibrium potentials are observed at ≈3.9 and 4.1 V versus Li^+/Li, which are concomitant with a transition of incorporated Li^+ from the 8*a* to 16*c* position in the host λ-MnO_2 structure.[7] However, lithium intercalation may not be the only charge storage mechanism operating in $LiMn_2O_4$, as suggested by EQCM measurements which indicate that less than one lithium ion is transferred per electron during electrochemical cycling of $LiMn_2O_4$.[5]

While $LiMn_2O_4$ is appealing as an electrode material for charge storage due to its high rate capabilities,[1] particularly at the nanoscale,[8,9] the practical use of $LiMn_2O_4$ for charge storage is limited by its lower capacity relative to other cathode materials. $LiMn_2O_4$ has a capacity of ≈110 mAh g^{-1}, while $LiCoO_2$ and $LiFePO_4$ have capacities of 140 and 170 mAh g^{-1}, respectively.[1] Furthermore, $LiMn_2O_4$ exhibits poor cycling capability, especially at elevated temperatures[10] and applying a potential <3.2 V versus Li^+/Li results in the irreversible formation of overlithiated $Li_xMn_2O_4$ where x is as high as 2.[5,7] Recent work has also indicated some reversibility at <3 V in nanoscale $LiMn_2O_4$, which is consistent with our observations below.[11,12]

Dr. M. J. Young,[+] Dr. A. M. Holder, Prof. C. B. Musgrave
Department of Chemical and Biological Engineering
University of Colorado
Boulder, CO 80309, USA
E-mail: charles.musgrave@colorado.edu
Prof. H.-D. Schnabel
Leupold-Institut für Angewandte Naturwissenschaften
Westsächsische Hochschule
08012 Zwickau, Germany
Dr. A. M. Holder, Prof. S. M. George, Prof. C. B. Musgrave
Department of Chemistry and Biochemistry
University of Colorado
Boulder, CO 80309, USA
Dr. A. M. Holder
National Renewable Energy Laboratory
Golden, CO 80401, USA
Prof. S. M. George
Department of Mechanical Engineering
University of Colorado
Boulder, CO 80309, USA
[+]Present address: National Institute of Standards and Technology, Boulder, CO 80305, USA

DOI: 10.1002/adfm.201602773

In order to improve these shortcomings and harness the high-rate charge storage in $LiMn_2O_4$, a detailed understanding of the origins of charge storage in nanoscale $LiMn_2O_4$ and the factors driving the degradation of $LiMn_2O_4$ is needed.

In this work, we provide new insight into the electrochemical behavior of $LiMn_2O_4$ using a unique experimental study combined with a theoretical analysis rooted in semiconductor and defect physics. The experimental study is enabled by a new method we developed for synthesis of thin-film $LiMn_2O_4$ by room-temperature electrochemical conversion of thin films of MnO. Thin films of MnO are grown by atomic layer deposition (ALD) using bis(ethylcyclopentadienyl)manganese ($Mn(CpEt)_2$) and water (H_2O) at 150 °C,[13] and are electrochemically oxidized and lithiated to $LiMn_2O_4$ at room temperature. The electrochemical conversion of MnO to $LiMn_2O_4$ was inspired by our previous work which demonstrated that ALD-grown MnO can be electrochemically oxidized to produce pseudocapacitive $NaMn_4O_8$ in aqueous electrolytes.[14]

$LiMn_2O_4$ synthesis is conventionally performed using solid-state reactions between sources of lithium and manganese, such as LiOH and MnO_2,[15] Li_2CO_3 and $Mn(NO_3)_2$,[16] or Li and MnO_2.[17] Other proven techniques for producing $LiMn_2O_4$ include molten salt synthesis[18] and sol-gel or hydrothermal synthesis.[19,20] Prior attempts to grow higher oxides of manganese by ALD produced ground-state β-MnO_2.[21] However, introducing alkali ions into films using soda-lime glass substrates enabled the formation of metastable α-MnO_2 by ALD.[22] More recently, spinel $LiMn_2O_4$ was synthesized using ALD of $Mn(thd)_3$, Li(thd), and ozone,[23] but required postdeposition annealing at 600 °C to activate the $LiMn_2O_4$.[23] The hybrid ALD-electrochemical method employed here to synthesize nanoscale thin-films of $LiMn_2O_4$ requires gentler processing than prior methods, while the ALD facilitates precise thickness control of the resulting $LiMn_2O_4$, which we leverage to study the mechanism of high-rate charge storage.

We also expand upon prior computational studies of the mechanism of charge storage in $LiMn_2O_4$ using our recently developed unified electrochemical band-diagram (UEB) framework that decouples the ionic and electronic insertion processes and evaluates the electronic insertion voltages independently of the elemental reference of the intercalating ion.[24] In contrast to existing techniques that calculate the reaction enthalpies for lithiation (the addition of both Li^+ and e^-) of the host material referenced to lithium metal to estimate the average operational potential,[25,26] the UEB framework leverages solid state physics and defect theory to quantitatively calculate the potentials where charge storage will occur and fundamentally understand the origins of charge storage as well as the driving forces for degradation in these thin films. See the Supporting Information for computational details. We have previously used the UEB framework to describe high-rate charge storage in pseudocapacitive α-MnO_2,[24] however this framework has not previously been applied to ion intercalation electrode materials. In α-MnO_2, high-rate charge storage was found to arise from electronic charge-switching that does not require compensating cation transport, a mechanism which we find to be operative in $LiMn_2O_4$ as well (vide infra).

Our theoretical study of $LiMn_2O_4$ also demonstrates the utility of the UEB framework to intelligently identify new candidate electrode materials for advanced batteries. This framework enables the fundamental connection of the intrinsic properties (e.g., band gap and work function) of λ-MnO_2 with the known equilibrium potentials of $LiMn_2O_4$ as depicted in **Figure 1**. These principles can be applied to assist in screening for electrode materials to be used with ionic liquid electrolytes which are stable at potentials up to 6V,[27,28] as well as emerging polymeric[29,30] and ceramic[31] solid-state electrolytes which show promise for possessing wider stable potential windows as depicted in Figure 1. Furthermore, the UEB framework allows for screening of the host material (here λ-MnO_2) to identify the range of expected equilibrium potentials independent of the cation of interest. This enables simultaneous screening for electrode materials in emerging battery technologies that use low-cost and earth-abundant singly charged cations (e.g., Na^+, K^+) and power-enhancing multiply charged cations (e.g., Mg^{2+}, Al^{3+}) as shown in Figure 1. The evaluation of candidate materials using the UEB framework, as exemplified herein for $LiMn_2O_4$, enables a robust approach for the computationally accelerated discovery of electrode materials for higher voltages and various cations.

2. Results and Discussion

2.1. MnO Growth on Stainless Steel

In this work, we observe a growth rate of 0.95 Å per cycle for ALD of MnO using $Mn(EtCp)_2$ and H_2O at 150 °C, in agreement with previous work.[13] See Section 2 in the Supporting Information for additional information regarding the growth and characterization of MnO.

2.2. Electrochemical Conversion

Following ALD deposition, MnO films were converted electrochemically as described below in the Methods Section. As

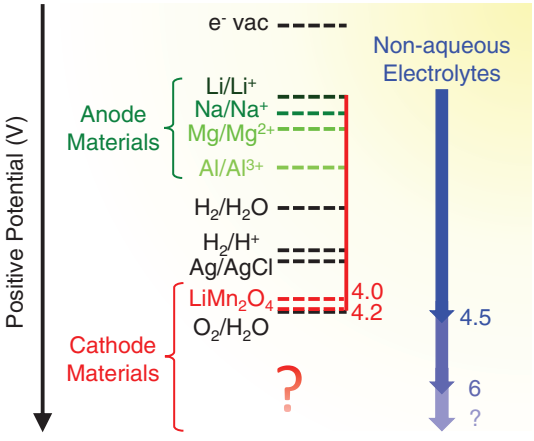

Figure 1. Absolute potential diagram motivating the need for high-voltage cathode materials, showing equilibrium potential regions for anodes (green) and cathodes (red), and electrolyte stability windows (blue), with common electrochemical references shown in black.

electrochemical treatment progresses, the electrochemical capacity (proportional to the area under the cyclic voltammetry (CV) curve) increases monotonically. One would expect that constant current oxidation alone would be sufficient to oxidize MnO to $LiMn_2O_4$. Surprisingly, although a constant current oxidation step was performed during electrochemical conversion, no change in capacity was observed immediately following this step. This suggests that successive oxidation/reduction steps during repeated voltage cycling CV measurements, not the fixed current oxidation, lead to the formation of $LiMn_2O_4$, in line with the incremental dissolution/reaggregation mechanism described below. During electrochemical conversion, two distinct peaks develop at ≈3.9 and ≈4.1 V versus Li^+/Li (≈0.7 and ≈0.9 V versus Ag/AgCl), as shown in **Figure 2**. These peaks exactly coincide with peaks that are commonly observed for $LiMn_2O_4$ and thus indicate that the electrochemical process converts the MnO film to $LiMn_2O_4$.[5,7] We also predict the origins and positions of these peaks theoretically, as described in detail below.

During electrochemical conversion of MnO, the pH of the electrolyte was measured repeatedly ex situ. We observed that the electrolyte pH decreased from 10 to as low as 6.5 during electrochemical treatment, indicating the production of acid during this process. Electrochemical water splitting or dissolution of MnO to Mn^{2+} is not expected to result in a net pH change. However, the decrease in pH is consistent with the formation of $LiMn_2O_4$, for example, by the overall reaction

$$Li_2SO_4 + 4MnO + 4H_2O \rightleftharpoons 2LiMn_2O_4 + 3H_2 + 2H^+_{(aq)} + SO^{2-}_{4(aq)} \quad (1)$$

and with formation of MnO_4^-, for example, by the overall reaction

$$MnO + 3H_2O \rightleftharpoons MnO^-_{4(aq)} + \frac{5}{2}H_2 + H^+_{(aq)} \quad (2)$$

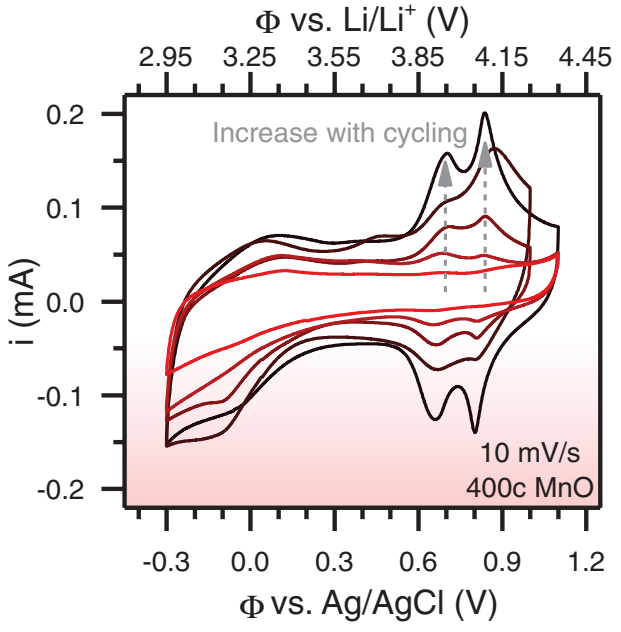

Figure 2. Cyclic voltammograms measured for 400 cycles MnO ALD (≈40 nm) on a stainless steel substrate in Li_2SO_4/Li_2CO_3 aqueous electrolyte at pH 10 during electrochemical conversion.

We note that reactions (1) and (2) are overall stoichiometric reactions for both electrodes, which include H_2O reduction on the counter electrode, and are not intended as mechanistic descriptors. When the measured pH was <9, dilute Li_2CO_3 was added to the electrolyte to maintain a pH of 9–11. We discuss the effect of pH on the electrochemical conversion of MnO to $LiMn_2O_4$ further below.

2.3. Film Characterization after Electrochemical Conversion

In addition to the presence of CV current peaks characteristic of $LiMn_2O_4$, the crystallinity and composition of the electrochemically treated MnO films verify the formation of $LiMn_2O_4$. **Figure 3**a shows grazing incidence X-ray diffraction (GIXRD) data, including diffractograms for both the ≈40 and ≈200 nm thick MnO films, following electrochemical treatment under basic conditions. Despite the small film thickness and the expected small crystallites, we observe distinct peaks in the GIXRD diffractogram which coincide with the reference diffractogram for $LiMn_2O_4$ and thus indicate electrochemical conversion of ALD MnO to spinel $LiMn_2O_4$. The crystal structure of

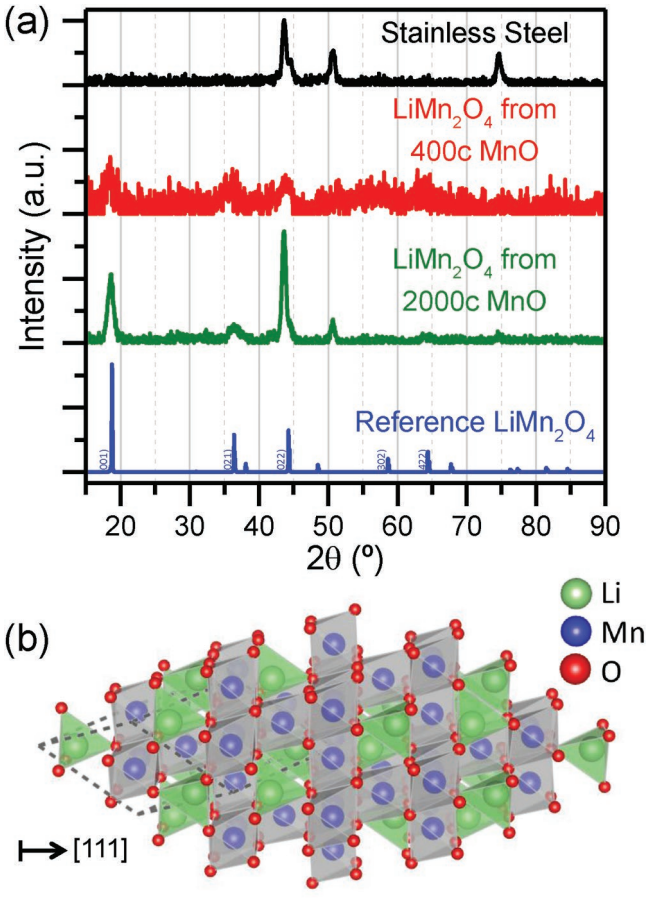

Figure 3. a) Grazing-incidence X-ray diffraction measurements of a bare stainless steel substrate, and $LiMn_2O_4$ films formed by electrochemical conversion of MnO films grown with 400 and 2000 MnO ALD cycles , including a reference diffractogram for b) the spinel $LiMn_2O_4$[43,57–59] crystal structure.

$LiMn_2O_4$ is shown in Figure 3b. The capacitance of the 40 nm MnO film following electrochemical oxidation to $LiMn_2O_4$ was ≈380 F g^{-1} over a 1.4 V window at a sweep rate of 1 mV s^{-1} (see the Supporting Information for additional detail). A higher capacitance of 570 F g^{-1} is observed from 0.5 to 1 V versus Ag/AgCl where the two peaks, labeled i_2 and i_3, are observed. This value corresponds to a capacity of 79 mAh g^{-1}, which approaches the value of 110 mAh g^{-1} expected for $LiMn_2O_4$.[1] The measured capacitance supports that we achieved at least 70% conversion of the 40 nm MnO film to $LiMn_2O_4$. The oxidation of MnO to the MnO_2 stoichiometry was also verified by X-ray photoelectron spectroscopy which indicated an O:Mn ratio of ≈2 throughout the depth of an electrochemically converted ≈100 nm film (See Section 3 in the Supporting Information for details).

The as-grown MnO films are flat, with roughnesses of ≈20 Å for the ≈40 nm MnO films as determined by X-ray reflectivity (XRR). However, following electrochemical oxidation, scanning electron microscopy (SEM) micrographs (**Figure 4**) show that the sample surfaces roughen and become nonuniform with some apparent submicron sized particles dispersed over the surface. Nevertheless, these topographical changes are modest considering the significant stoichiometry and phase changes that occur during electrochemical treatment. We note that the samples shown in Figure 4 were rinsed with deionized water prior to SEM imaging to remove any contamination from electrochemical treatment.

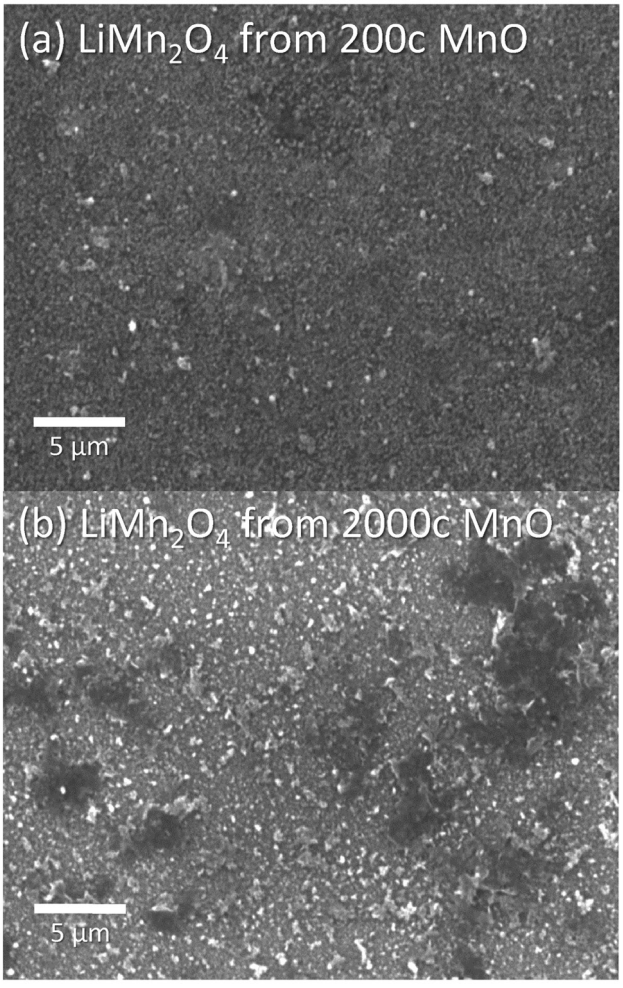

Figure 4. Scanning electron microscopy micrographs after electrochemical conversion to $LiMn_2O_4$ for initial MnO deposited by a) 200 ALD cycles, and b) 2000 ALD cycles.

2.4. Quantum Mechanical Calculations

We evaluated the cation incorporation charge storage mechanism in $LiMn_2O_4$ using the UEB approach,[24] which couples an ab initio description of the electronic structure of the defect states induced by ion incorporation into the host structure with an electrochemical description of the electrode interface. This approach predicts the presence, nature, and potentials of charge switching states and thus the locations, origins, and relative magnitudes of features in a CV that arise from reduction and oxidation of these states.

The UEB approach involves using the work function and band gap of the host material, here λ-MnO_2, to determine the absolute band energies of the host material as a reference for successive calculations with incorporated ions. The structure of the perfect host λ-MnO_2 structure devoid of Li^+ cations is illustrated in **Figure 5**a. A plot of the calculated plane-averaged local Hartree potential versus position along the [111] direction of a slab of the λ-MnO_2 host structure with the dominant (111) termination[32] is displayed in Figure 5b. The blue curve represents the bulk material and the black curve represents the slab with vacuum space, where we aligned the two potentials using the average local Hartree potential of the bulk material $\left(V_{avg}^{bulk}\right)$. The work function for the host material is defined as the energy difference between the bulk Fermi level and an electron in vacuum.[33] We calculate the λ-MnO_2 host material work function to be 8.0 eV, which we use to plot the projected density of states (PDOS) on an absolute energy scale versus an electrochemical reference as illustrated in Figure 5c. This work function is calculated for defect-free λ-MnO_2. As discussed below, incorporation of interstitial lithium introduces occupied electronic states near the conduction band edge, resulting in a predicted experimental work function of ≈6 eV for $LiMn_2O_4$, in close agreement with the experimental work function of 6.2 eV calculated from ultraviolet photoelectron spectroscopy data.[34] The PDOS indicates that the valence band is primarily composed of O[2p] character while the conduction band is primarily composed of Mn[3d] character and current peaks are predicted to appear near the bottom of the electrochemically scanned region (2.95–4.35 V versus Li^+/Li), just below the conduction band edge of the host λ-MnO_2 electronic structure. We also calculate a 2.3 eV indirect band gap for the host λ-MnO_2 structure.

Our previous study of α-MnO_2[24] suggested that cations intercalate into the host λ-MnO_2 structure and interact with antibonding Mn—O orbitals to stabilize them from the conduction band into the band gap. Thus, we expect that the resulting cation-induced defect states fall within ≈1 eV of the conduction band edge and switch charge state as the cycled potential sweeps the Fermi level past their electronic energies, thus giving rise to the observed peaks in the CV. However, using the conven-

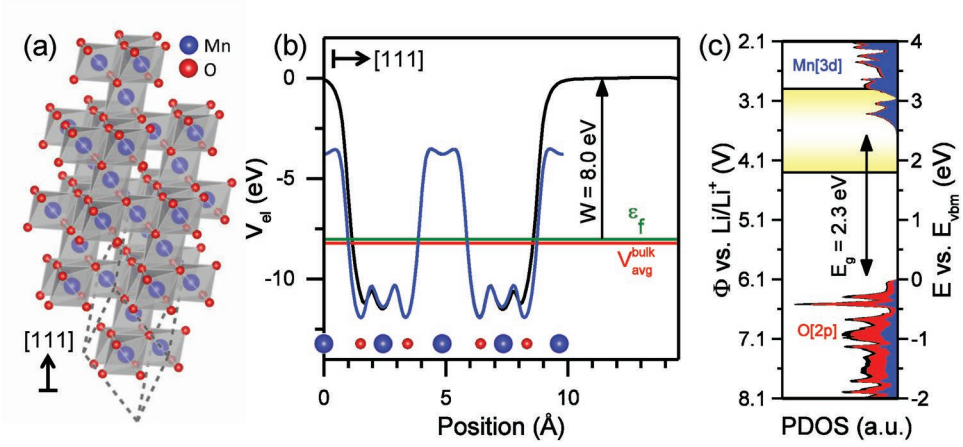

Figure 5. a) Calculations of host λ-MnO_2 devoid of lithium,[58] including b) plane-averaged local Hartree potential in the [111] crystallographic direction for bulk (blue), and slab (black) λ-MnO_2 with the Fermi energy, ε_f, average bulk potential, V_{avg}^{bulk}, and work function, W, indicated. The blue and red circles denote the in-plane presence of O and Mn, respectively. c) The projected density of states of bulk λ-MnO_2 at energies referenced to Li^+/Li and the valence band maximum energy, E_{vbm}, of λ-MnO_2. Oxygen character is shown in red and manganese character is shown in blue. The experimentally scanned potential region is highlighted in yellow.

tional rigid band model (which neglects explicit evaluation of varying charge states of the fully lithiated λ-Mn_2O_4 host structure), the positions of these defect levels in $LiMn_2O_4$ cannot be quantitatively stated. Thus, we can only anticipate that as in α-MnO_2, cations will induce charge-switching states with equilibrium reduction potentials at electronic energies that lie below the conduction band minimum, ≈1 eV below the band edge.

By performing total energy calculations of the fully lithiated $LiMn_2O_4$ structure, we are able to more precisely predict the electrochemical behavior of $LiMn_2O_4$. **Figure 6** presents a comparison of experimental CV measurements with the theoretically predicted potentials derived using the UEB method, as well as a qualitative PDOS diagram. Note that although the PDOS diagram was determined using the Heyd-Scuseria-Ernzerhof range-separated hybrid functional (HSE06) method, it does not align with the predicted potentials. This is because this PDOS is derived from a calculation for one charge state (rigid band model) and does not accurately account for all of the factors required to quantitatively determine the potentials for transitions between charge states.

While we previously investigated a variety of cations incorporated into the crystal structure of α-MnO_2, including protons, here, we primarily focus on lithium ions due to the prevalence of $LiMn_2O_4$ as a cathode material for lithium ion batteries. While we discuss the effects of exchanging Li^+ for Na^+, K^+, and Mg^{2+} (vide infra), we expect negligible contribution from protons at the basic conditions primarily examined in this work. We also previously suggested that defect interactions in α-MnO_2 resulted in equilibrium-potential smearing. While this likely plays a role in $LiMn_2O_4$ as well, we expect the broadening of cation defect levels are limited due to the more shielded and isolated environment of cations incorporated in the λ-MnO_2 host structure.

A comparison of the CV and the UEB calculated charge-switching potentials of $LiMn_2O_4$ depicted in Figure 6a,b shows that the electronic transitions of fully lithiated $LiMn_2O_4$ serve as a reliable predictor of the experimental equilibrium potentials for charge transfer. As we anticipated above, these predicted electronic transitions arise from the stabilization of conduction band states of the host λ-MnO_2 upon incorporation of

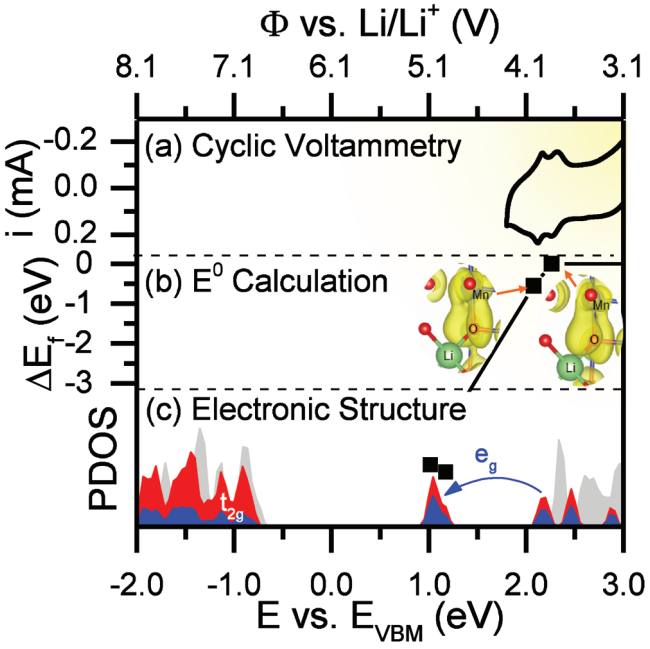

Figure 6. Comparing calculations and measurements on $LiMn_2O_4$. a) CV measurement on 400 cycles of MnO ALD after electrochemical conversion to $LiMn_2O_4$ in basic electrolyte. b) UEB calculated formation energies for various charge states of $LiMn_2O_4$ with charge-switching potentials, E^0, indicated by square symbols. The inset images show the band-decomposed charge densities of the corresponding Mn—O orbitals involved in charge storage. c) Density of states at the Γ-point of the host λ-MnO_2 (grey), and O (red) and Mn (blue) components of $LiMn_2O_4$. The locations of the states in (c) do not align with (a) and (b) due to the incomplete description of the single calculation used in generating (c), hence the necessity of performing the multiple calculations necessary in deriving (b).

Li^+ cations, as depicted in Figure 6c. The field of the positively charged Li^+ favorably interacts with the conduction band states of MnO_2, composed predominantly of $Mn(e_g)$-O(2p) character, by localizing them to the neighboring Mn—O octahedra and stabilizing their energy into the band gap.

The inset of Figure 6b shows a band-decomposed charge density analysis of the stabilized states that accept electrons when an applied potential raises the Fermi level above these states. The insets show that the two defect bands arising from interaction of Mn—O antibonding states with Li^+ differ in their orientation with respect to the intercalated Li^+. In this position, a lobe of the higher energy band is pointed directly at the Li^+ interstitial, whereas the lobes of the lower energy band straddle the lithium center. In these images, Li^+ coordinates to four oxygen atoms where bonds are illustrated only for directional reference, and do not indicate covalent bond character. The differing interactions with Li^+ that split these bands are analogous to differences in the interactions that give rise to e_g-t_{2g} crystal field splitting, which we propose is the fundamental basis for the experimental observation of two separate equilibrium potentials at ≈3.9 and ≈4.1 V versus Li^+/Li. Future work will more comprehensively examine the utility of employing crystal field theory to understand the electrochemical behavior of this and other battery materials.

The band-decomposed picture also provides insight into the migration of Li^+ from the 16*c* to the 8*a* position under applied positive potential as has been observed experimentally.[7] In the fully intercalated $LiMn_2O_4$ structure, the Li^+ interstitials occupy the 16*c* position. At potentials <≈4.1 V versus Li^+/Li, the higher energy band, as depicted in the right-hand inset of Figure 6b, is occupied and stabilizes Li^+ in the 16*c* position. However, at potentials >≈4.1 V versus Li^+/Li, the higher energy lobe is unoccupied and Li^+ is repelled from the adjacent Mn—O group toward the 8*a* position. The migration of Li^+ between these sites is expected to occur slowly, requiring removal of half of the Li^+ from the bulk structure, while the electronic occupation of these orbitals is expected to occur rapidly because it only requires electron transport.

2.5. pH Dependence of Electrochemical Conversion

Cyclic voltammograms scanned at 20 mV s^{-1} for various film thicknesses following 60 CV cycles at a pH of ≈6 are presented in **Figure 7**a. CV traces taken during electrochemical conversion at this pH are shown in Figure S4 of Section 4 (Supporting Information). At this mildly acidic pH condition, conversion to $LiMn_2O_4$ is evident by the appearance of peaks at ≈3.9 and

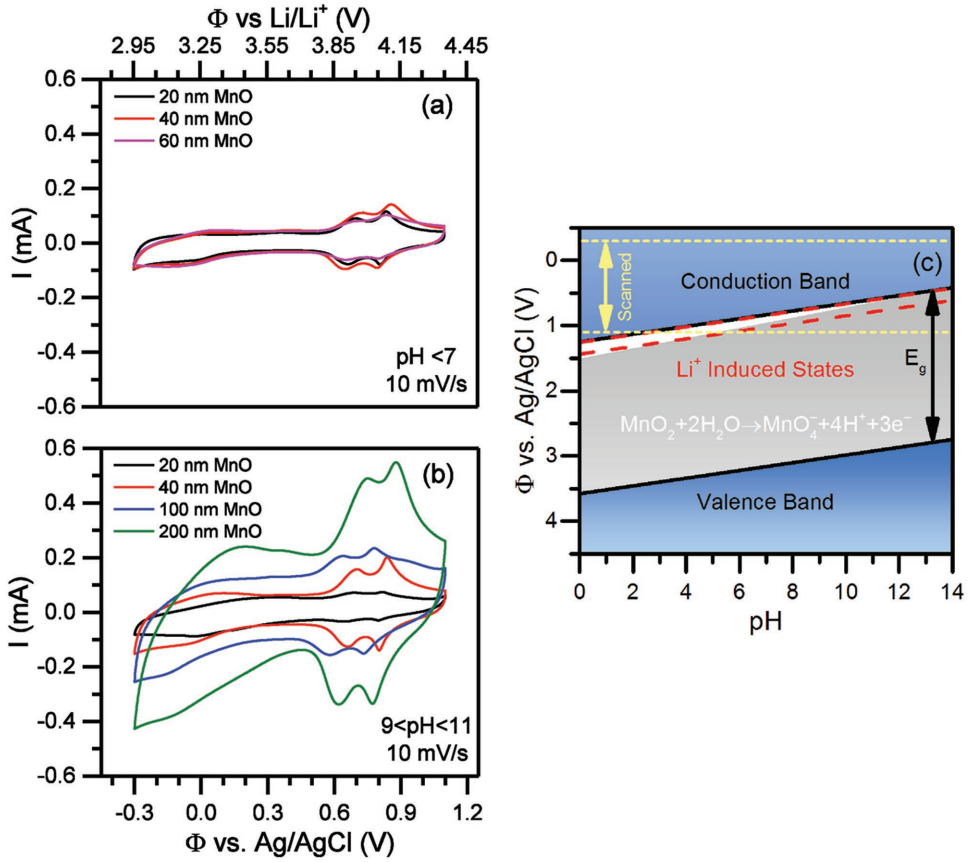

Figure 7. Impact of pH on electrochemical conversion, including cyclic voltammograms for varying thicknesses of MnO following electrochemical treatment in a) mildly acidic 0.1 M $Li_2SO_{4(aq)}$ electrolyte, and b) basic electrolyte buffered to a pH of 10 using Li_2CO_3. As well as c) Pourbaix-like diagram depicting the UEB calculated band edges of λ-MnO_2, charge-switching potentials for $LiMn_2O_4$, and the boundary for thermodynamically favorable decomposition of MnO_2 to MnO_4^- as a function of pH.

≈4.1 V versus Li^+/Li in Figure 7a. However, the shape and area under the CV curves for three film thicknesses are nearly identical. This indicates that electrochemical treatment in mildly acidic electrolyte does not convert the entire film to $LiMn_2O_4$, but perhaps instead converts only a constant quantity (≤20 nm) of MnO to $LiMn_2O_4$ which provides the electrochemical capacitance. This is in sharp contrast to the trend in capacity versus film thickness for MnO films oxidized under basic conditions, as shown in Figure 7b. For basic conditions, the area under the CV curve, as well as the peak heights, increase monotonically with increasing film thickness.

While protons are expected to be present in low concentrations at the mildly acidic conditions in Figure 7a, we suggest that the charge storage we measure in Figure 7a arises primarily from Li^+ in λ-MnO_2. Our prior work predicted that as much as 50% of charge storage in α-MnO_2 arises from protons which incorporate at sites in α-MnO_2 where larger cations are sterically hindered.[24] Conversely, in λ-MnO_2 Li^+ readily occupies all of the cation-incorporation sites. While protons may compete with Li^+ for interstitial sites in λ-MnO_2 under kinetically limiting conditions, Li^+ insertion is expected to be more favorable at equilibrium. This is supported by the observation that protons incorporate into λ-MnO_2 only in the presence manganese vacancies.[35] Occupation of Mn vacancies by protons is expected to shift the equilibrium potential for charge storage.[24] Furthermore, while protons may contribute to charge storage under acidic conditions, any manifestation of this is obfuscated by the incomplete conversion of MnO to $LiMn_2O_4$ under acidic conditions. We note that this discussion is only relevant to acidic conditions and therefore the results we report in Figure 7a, and that protons do not contribute significantly to charge storage at the basic conditions primarily used in this work.

The influence of pH on the electrochemical conversion of MnO can be understood by employing a Pourbaix-like diagram as shown in Figure 7c. This figure differs from a standard Pourbaix diagram in that the γ-axis shows increasingly negative potentials for increasing γ, such that higher electron energies correspond to a greater γ-value. Also, this diagram plots the band edges of the host λ-MnO_2 structure, the predicted equilibrium potentials for charge switching in $LiMn_2O_4$ and the relevant decomposition reactions of MnO_2 as a function of pH. We note that the surface of MnO will readily convert to MnO_2 under atmospheric conditions,[13,36,37] and therefore we examine the electrochemical properties of MnO_2 in Figure 7c to understand the electrochemical conversion of MnO to $LiMn_2O_4$. Figure 7c shows that at any particular pH, the oxidative decomposition of MnO_2 to form permanganate (MnO_4^-) by the reaction

$$MnO_2 + 2H_2O \rightleftarrows MnO_4^- + 4H^+ + 3e^- \quad (3)$$

becomes more thermodynamically favorable with increasing positive potentials.

We suggest that the pH-dependence of the favorability of MnO_4^- formation by reaction (3) leads to the differences in the thickness of MnO converted to $LiMn_2O_4$ shown in Figure 7. At basic pHs, reaction (3) becomes favorable within the scanned potential range. For example, at a pH of 10 MnO_4^- formation is favored at potentials >0.75 V versus Ag/AgCl, as depicted in Figure 7c. At this pH, as the potential is swept into the grey region, reaction (3) will be driven forward. Reaction (3) is expected to proceed by adsorption of H_2O to form surface manganese complexes of higher oxidation state with adsorbed −OH intermediates, followed by dissolution of surface manganese as MnO_4^-. These processes should lead to dynamic roughening and etching of the film surface, enabling penetration of lithium and water into the bulk manganese oxide film. As the potential is scanned out of the grey region, reaction (3) will be driven in reverse, leading to redeposition of dissolved Mn by readsorption of MnO_4^- and reduction of these higher oxidation state surface manganese complexes to again form $LiMn_2O_4$. Therefore, at a pH of 10, repeated CV cycling will lead to the conversion of MnO to $LiMn_2O_4$, as depicted in Figures 2 and 7b.

Conversely, at the acidic pHs shown in Figure 7a, the potential is not scanned into the grey region. Therefore, any MnO_2 present in the film remains stable and formation of $LiMn_2O_4$ is limited to the near-surface region of the manganese oxide film, corresponding to the depth that water and lithium are able to penetrate into the relatively static and dense MnO_2 film. We note that the theoretical predictions in Figure 7c are derived from the UEB framework and allow for the interpretation of the experimental results for electrochemical conversion of MnO to $LiMnO_2$ in Figure 7a,b.

Therefore, the conversion of MnO to MnO_2 is suggested to proceed via a multistep process, where (a) surface MnO spontaneously reacts with H_2O to form a thin-film of MnO_2, (b) MnO_2 oxidizes to form MnO_4^- under positive potentials and the underlying MnO is partially oxidized, and (c) MnO_4^- is reduced on the surface under negative bias in the presence of Li^+ from the electrolyte to form $LiMn_2O_4$. This mechanism is supported by our observations that CV cycling is necessary to form $LiMn_2O_4$ and that the extent of conversion to $LiMn_2O_4$ is pH-dependent. The importance of the pH and permanganate ion as well as the dissolution and aggregation growth process we describe is also consistent with previous results on hydrothermally grown manganese oxide polymorphs.[38]

The Pourbaix-like construct also provides a fundamental understanding of the slow conversion of $LiMn_2O_4$ to $Li_{1+\delta}Mn_2O_4$ at more negative potentials. As the bias applied to the λ-MnO_2 is scanned to potentials more negative than the redox potentials for charge switching of intercalated Li^+, electrons begin to populate and possibly localize the low lying conduction band states of the λ-MnO_2 that lie just above the potentials of the Li^+ induced defect states (see Figure 6). Consequently, the $LiMn_2O_4$ film is expected to undergo Fermi-level pinning at the conduction band edge, where the accumulation of negative charge drives the reduction of $LiMn_2O_4$ to $Li_{1+\delta}Mn_2O_4$.[5,7] We expect this process to be slow as it requires a bulk rearrangement of atoms to form the new crystal structure.[5] We emphasize that this thermodynamic analysis using the Pourbaix-like construct can be applied in an arbitrary electrolyte or interfacial environment, provided that the chemical potential of a proton (i.e., pH) in this environment can be determined.

2.5.1. Deconvolution of Capacitive and Diffusive Charge Storage

In addition to the broad implications for understanding charge storage in battery materials obtained from the UEB construct,

the accurate prediction of the observed equilibrium potentials by our ab initio electronic structure calculations suggests that a fraction of the electronic charge storage in $LiMn_2O_4$ could originate from an electronic insertion process that is decoupled from the ionic insertion process and therefore stores charge without mass transport of lithium. To evaluate this possibility, we delineated the capacitive and diffusive contributions to charge storage in $LiMn_2O_4$ films of different thicknesses using an electrochemical analysis based on varying the sweep rate to eliminate contributions from diffusive processes that occur on long timescales relative to the sweep rate. Here, capacitive contributions to charge storage include (a) double-layer capacitance, (b) dielectric capacitance, and (c) electronic charge-switching without compensating mass transport of Li^+. In contrast, diffusive contributions to charge storage require ionic mass transport. Sections 5 and 6 (Supporting Information) describe an analysis of the total capacitance of $LiMn_2O_4$ versus film thickness that does not distinguish between capacitive and diffusive components. **Figure 8**a shows the mass-averaged oxidation current, i_{avg}, as a function of sweep rate for various starting MnO thicknesses after electrochemical conversion to $LiMn_2O_4$ on a log–log scale. To calculate i_{avg}, an arithmetic mean of the current on the oxidation sweep was used to represent the average amount of charge storage over the 1.4 V window and the mass of $LiMn_2O_4$ was calculated from MnO XRR thicknesses and densities assuming complete conversion to $LiMn_2O_4$. The analysis in Figure 8 was performed based on a power-law expression for the current, i, versus sweep rate, ν

$$i = a\nu^m \tag{4}$$

where, a and m are constants and m corresponds to the slope of a log–log plot of current versus sweep rate as depicted in Figure 8a. Using a constant phase element description of the charge storage processes,[39] the value of m can vary freely between the limits of 0.5 and 1, which correspond to diffusive and capacitive processes, respectively.[40] Figure 8a also depicts bounding conditions for the slope corresponding to ideal capacitive and diffusive processes. The fraction of diffusive charge storage, f_d, is determined using the expression

$$f_d = \frac{1-m}{0.5} \tag{5}$$

which is used to calculate the capacitive and diffusive contributions in Figure 8b. This analysis expands on existing methods

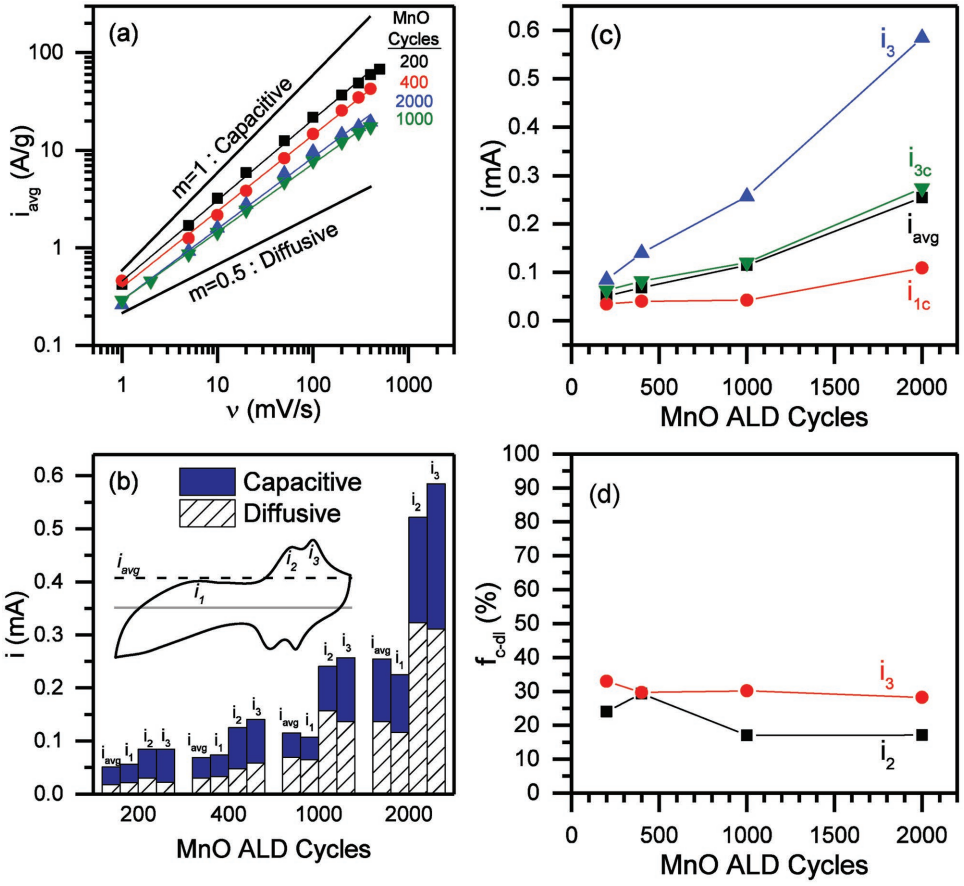

Figure 8. Contributions to charge storage for varying MnO thicknesses after electrochemical conversion to $LiMn_2O_4$ in basic electrolyte including: a) Log–log plot of average current versus sweep rate for deconvolution of capacitive and diffusive contributions to measured current. b) Deconvolution of the capacitive and diffusive contributions at various potentials on the CV curve, as depicted in the inset figure. c) Contributions to measured current during CV experiments versus the initial number MnO ALD cycles. d) Nonsurface capacitive contributions to the measured current, indicative of bulk charge-switching. The currents i_1, i_2, and i_3 are indicated on the voltammogram shown in the inset of (b).

to separate capacitive and diffusive charge storage using expressions of current versus sweep rate,[40,41] as described in more detail in the Supporting Information of ref. [14].

The values of slopes for the traces in Figure 8a are 0.83, 0.78, 0.73, and 0.70 for the 20, 40, 100, and 200 nm samples, respectively. Although the capacity of the $LiMn_2O_4$ film derived from 200 ALD MnO cycles (≈20 nm thickness) is much larger than that of the bare stainless steel substrate (see Figure S5, Supporting Information), the processes leading to charge storage occur rapidly. Hence, the slope of the trace in Figure 8a for the $LiMn_2O_4$ film derived from 200 ALD MnO cycles illustrated lies close to the ideal double-layer curve. This behavior arises from a large surface area to volume ratio for this thin film. For thicker films, a larger fraction of charge storage arises from diffusion-limited bulk processes. For the $LiMn_2O_4$ films derived from 1000 and 2000 MnO ALD cycles (≈100 and ≈200 nm thicknesses, respectively), the slope of the current versus sweep rate lies much closer to the ideal slope for a diffusion limited process, although capacitive charge-storage still contributes a large fraction to the total charge-storage. These results agree with the current understanding of the charge storage mechanism of $LiMn_2O_4$ outlined in the introduction, and suggest that thinner films result in higher specific mass capacities and rates due to the higher fractional contribution from surface capacity, and faster ion transport than in thicker films, respectively.

A more in-depth analysis of the current at various potentials in the CV curve elucidates unique mechanistic behavior. Figure 8b presents an analysis of the capacitive and diffusive contributions to the measured current for varying thicknesses of $LiMn_2O_4$, and at various points in the CV curve. Here, i_1 is the peak current observed at ≈0.1 V versus Ag/AgCl, i_2 is the peak current observed at ≈3.9 V versus Li^+/Li, and i_3 is the peak current observed at ≈4.1 V versus Li^+/Li. The overall increase in i_{avg} at larger thicknesses corresponds to the bulk conversion to $LiMn_2O_4$ at basic pHs, as described above for Figure 7b, while the more dramatic increase in peak currents i_2 and i_3 indicates that this higher capacity arises mainly from the charge-storage processes at the two equilibrium potentials. Thus far, this is consistent with existing mechanistic descriptions of charge storage in $LiMn_2O_4$.

However, the prevailing picture of charge storage ascribes nearly all of the observed current at i_2 and i_3 to diffusive processes and requires one Li^+ to diffuse out of the material for each electron removed from the cathode. Instead, a large capacitive contribution, denoted with a subscript *c*, is observed for i_2 and i_3 for all $LiMn_2O_4$ thicknesses. If these capacitive contributions i_{2c} and i_{3c} were solely due to double-layer processes, we would expect a constant capacitive over the potential window with $i_{3c} = i_{2c} = i_{1c}$. However, i_{3c} is greater than i_{1c} for all MnO thicknesses, as depicted in Figure 8c, surpassing even the total average current, i_{avg}! This suggests that an additional capacitive process distinct from the surface double layer capacitance contributes to rapid charge storage.

By assuming that i_{1c} is equivalent to the current arising from the surface double-layer at each thickness, and that this current is constant over the whole potential range, the fraction of capacitive current contributed by non-double-layer processes, f_{c-dl}, can be calculated for both i_2 and i_3. For instance, the capacitive fraction f_{c-dl} at peak i_3 can be calculated as $f_{3cdl} = (i_{3c} - i_{1c})/i_3$. The percentages of i_2 and i_3 due to nonsurface capacitive processes, i.e., dielectric and bulk charge-switching, for four $LiMn_2O_4$ thicknesses are presented in Figure 8d. We expect dielectric contributions to be negligible, and estimate from Figure 8d that ≈20% of i_2 and ≈30% of i_3 arise from bulk electronic charge-switching processes.[24]

In addition to the double layer capacitance we account for above, some portion of the rapid charge-switching in Figure 8d is expected to arise from rapid faradaic reactions on the surface of the $LiMn_2O_4$. However, the contribution of these surface processes does not account for the capacitive charge storage we observe. Over the potential window from 0.5 to 1 V versus Ag/AgCl, we measure a capacitive portion of charge storage at a sweep rate of 10 mV s^{-1} corresponding to 103 F g^{-1} for the $LiMn_2O_4$ sample converted from 2000 MnO ALD cycles. The combination of double layer capacitance and surface faradaic reactions are expected to give rise to ≈100 μF cm^{-2} of charge storage in MnO_2.[42] Using this value, this ≈200 nm $LiMn_2O_4$ film would need to have a specific surface area of ≈100 m^2 g^{-1} in order for surface processes to account for the capacitive contribution we measure. Taking the density of $LiMn_2O_4$ to be 4 g cm^{-3} as calculated from the international crystal structure database structure,[43] 100 m^2 g^{-1} corresponds to a uniform distribution of $LiMn_2O_4$ particles with a 15 nm diameter. For thinner $LiMn_2O_4$ films and lower sweep rates, this calculated specific surface area is larger still. The largest value we calculate of 230 m^2 g^{-1} is for the ≈40 nm $LiMn_2O_4$ film thickness at a sweep rate of 1 mV s^{-1} and corresponds to a uniform distribution of 6 nm particles. While we observe slight surface roughening in Figure 4, we do not observe a dramatic morphology change consistent with feature sizes of ≈10 nm. The smallest particles visible in Figure 4 are ≈100 nm in diameter, and the particles are only sparsely dispersed on the surface. Even a dense distribution of 100 nm $LiMn_2O_4$ particles would provide a surface area of only ≈15 m^2 g^{-1}, an order of magnitude smaller than necessary for surface processes to account for the capacitive charge storage we observe.

Furthermore, the capacitive contribution of i_{1c}, i_{2c}, and i_{3c} are not consistent with an increase in surface area, further supporting the bulk capacitive mechanism we describe. If the capacitive contribution arose from surface processes, the capacitive contribution of all three peaks (i_{1c}, i_{2c}, and i_{3c}) would be proportional to the surface area of each sample. Because i_{1c}, i_{2c}, and i_{3c} are greater for larger thicknesses, this would imply that thicker $LiMn_2O_4$ samples simply have greater surface areas. However, our data indicate that i_{1c}, i_{2c}, and i_{3c} do not increase uniformly with increasing film thickness and therefore the capacitive charge storage cannot only be due to an increase in surface area. The capacitive contribution from i_1 is 35 μA for the thinnest $LiMn_2O_4$ sample and approximately three times greater at 109 μA, for the thickest $LiMn_2O_4$ sample. In contrast, the capacitive contribution from i_3 is 63 μA for the thinnest $LiMn_2O_4$ sample and approximately four times greater at 274 μA for the thickest $LiMn_2O_4$ sample. The greater increase in i_{3c} indicates a bulk capacitive contribution to i_3.

The above analysis suggests that up to ≈30% of rapid charge storage in nanoscale $LiMn_2O_4$ is due to bulk electronic charge-switching that does not require transport of Li^+ to compensate charge, in agreement with our theoretical calculations. Instead, electrons are expected to rapidly occupy and vacate a portion

of the available electronic states depicted in Figure 6, limited only by the extent to which charge accumulation is stable in the λ-MnO_2 host. This stable accumulation of charge is analogous to stable charged dopants in semiconductor applications. The λ-MnO_2 host dielectrically screens the positive charge, stabilizing it in the structure. When the extent of charge accumulation exceeds what the λ-MnO_2 host can accommodate, Li^+ will migrate into or out of the $LiMn_2O_4$ structure as necessary to balance charge. Our experimental measurements suggest that this bulk electronic charge-switching mechanism accounts for up to 20%–30% of the total capacity, conspicuously close to the 27% of residual Li left in $LiMn_2O_4$ upon complete discharge[5,44] and the ≈20% of Mn centers which are thought to contribute to the rapid charge-storage in pseudocapacitive α-MnO_2 with incorporated Na^+.[24,45] This interpretation also explains previous EQCM measurements on $LiMn_2O_4$ which measure a mass per electron value of as low as 4 g mol^{-1} e^- during electrochemical cycling of $LiMn_2O_4$.[6] If one lithium ion is removed for each electron, the expected value is 7 g mol^{-1} e^-. The ≈40% lower mass change agrees with the 20%–30% of bulk charge-switching capacity we calculate from our measurements and corroborates our interpretation that 20%–30% of the capacity of $LiMn_2O_4$ does not require mass transport of Li^+ at the sweep rates of 1–400 mV s^{-1} we examine in this work.

2.6. Replacing Lithium with Other Cations

Figure 9 shows cyclic voltammograms for $LiMn_2O_4$ as measured in various aqueous electrolytes containing different cations. For these experiments, 0.1 M Li_2SO_4, Na_2SO_4, K_2SO_4, and $MgSO_4$ electrolytes were used with the pH of each tuned to 10 using each cation's corresponding carbonate. The use of H_2SO_4 electrolyte

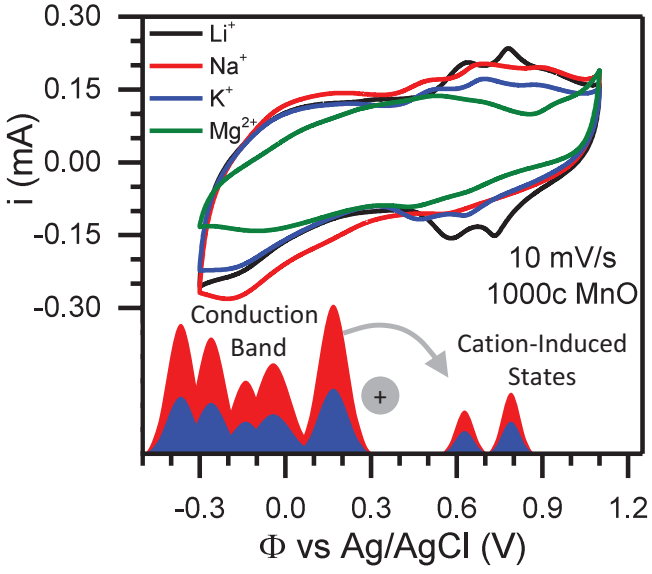

Figure 9. CV measurements in 0.1 M Li_2SO_4, 0.1 M Na_2SO_4, 0.1 M K_2SO_4, and 0.1 M $MgSO_4$ buffered to a pH of 10 using the carbonate of each salt, measured on a sample of 1000 cycles of MnO ALD following electrochemical conversion to $LiMn_2O_4$. A qualitative density of states of λ-MnO_2 upon cation incorporation is depicted in the inset.

is precluded by instability of $LiMn_2O_4$ at pH < 4.[46,47] The same $LiMn_2O_4$ sample was transferred to different electrolyte solutions and CV curves were measured in each electrolyte. We observed small, but distinct differences between the cations; in Na^+ and K^+ electrolytes a third peak is observed within the same region where we measured two peaks in the Li^+ electrolyte, and no peaks are observed in this region in the Mg^{2+} electrolyte.

Differences in these CVs are expected to arise due to differing interactions of the various cations of the electrolyte with the host λ-MnO_2 structure. Li^+ has an ionic radius of 0.59 Å, while Na^+ and K^+ have larger radii of 0.99 and 1.37 Å, respectively.[48] These larger radii are expected to have two separate effects. First, incorporation of these larger cations causes an expansion of the host MnO_2 that distorts the symmetry and consequently changes the crystal field interactions between the cation and the perturbed orbitals that comprise the conduction band minimum. We suggest that this effect gives rise to the three peaks we observe in the cases of Na^+ and K^+ rather than the two peaks observed for the case of Li^+. Second, these interstitial cations associate at a greater distance from oxygen atoms in the host due to their larger radii, resulting in weaker interactions with the MnO_2 host as compared to Li^+. Hence, these cations do not stabilize the conduction band states as far into the band gap, which explains why in Figure 9 a peak is observed at a more negative potential for these cations than was observed for the case of Li^+.

In contrast, at 0.57 Å, Mg^{2+} has a smaller ionic radius[48] than Li^+ and double the positive charge, leading to a stronger positive field surrounding Mg^{2+}. This contributes to a large exothermic Gibbs energy of hydration (ΔG_{hyd}) for Mg^{2+} of –19 eV.[49] This value is three to five times larger than values reported for Li^+, Na^+, and K^+, which are –5.8, –4.6, and –3.9 eV, respectively.[49] The stability of the Mg^{2+} solvation shell suggests that shedding solvent is energetically prohibitive and may inhibit Mg^{2+} from incorporating into the host MnO_2 at potentials where charge-switching is favored. If Mg^{2+} does shed its solvation shell and incorporates into the host MnO_2 at potentials where charge-switching is favored, its stronger field will stabilize conduction band states farther into the band gap and result in equilibrium potentials at more positive potentials than were observed for Li^+. The absence of a peak in the range of 3.8–4.2 V versus Li^+/Li is consistent with the prediction that Mg^{2+} does not incorporate into MnO_2, however we were unable to determine the presence of peaks at more positive potentials with the experiments presented herein due to the oxidative decomposition of water at potentials >1.1 V versus Ag/AgCl.

Additionally, we performed an equivalent analysis to that illustrated in Figure 8 to determine the surface double-layer, bulk capacitive, and mass-transport-limited fractions of the peak current for each cation by varying the CV sweep rate from 1 to 400 mV s^{-1}. The results of this analysis (presented in **Figure 10**) shows that a significant portion (22%–35%) of the peak current arises from bulk charge-switching in each electrolyte. This may arise from bulk charge-switching tied to each type of cation, but considering the relatively constant value of this bulk capacitive contribution to current, we suggest that it originates from residual Li^+ present in the initially lithiated MnO_2 host throughout the experiments. Further analysis outside of the scope of this work will be required to distinguish the

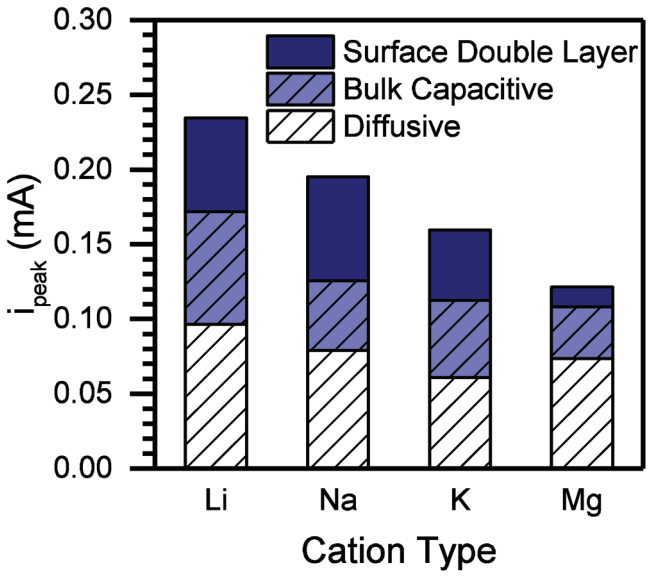

Figure 10. Peak current decomposed into surface double-layer, bulk capacitive, and diffusive contributions versus the cation used in the electrolyte on a sample of 1000 cycles of MnO ALD following electrochemical conversion to $LiMn_2O_4$.

nature of bulk charge-switching for various types of intercalated cations.

3. Conclusions

In this work, we demonstrate a novel approach to the synthesis of spinel $LiMn_2O_4$ by room temperature electrochemical oxidation and lithiation of ultrathin ALD-MnO films in aqueous lithium electrolyte. We determine that this conversion is pH-dependent, with ≤20 nm of MnO converting to $LiMn_2O_4$ in a mildly acidic electrolyte and as much as 200 nm of MnO converting to $LiMn_2O_4$ at a pH of ≈10. We suggest that the pH dependence of the conversion of $LiMn_2O_4$ arises from a corresponding pH-dependence of the thermodynamic favorability of MnO_4^- formation. At more basic pHs, MnO_4^- is more thermodynamically stable than MnO_2 for a fraction of the scanned potential range, resulting in the conversion of surface MnO to $LiMn_2O_4$ through a dissolution and aggregation growth process. This synthesis strategy can be reapplied to other metal oxide systems, enabling controlled thin-film synthesis of other metastable phases.

Additionally, by employing our newly developed unified electrochemical band diagram framework to analyze the charge storage mechanism of $LiMn_2O_4$, we identify charge switching of the Li^+-stabilized conduction band states of the host λ-MnO_2 as the source of the two observed reduction potentials in $LiMn_2O_4$. This work represents the first time the UEB framework that has been used to study charge storage of an ion intercalation material. A traditional band diagram description of the host λ-MnO_2 predicts a single, averaged reduction potential at ≈4.0 V versus Li^+/Li. The UEB framework is able to more accurately capture the mechanism of charge storage in $LiMn_2O_4$ by leveraging fundamental solid state physics and defect theory. The UEB analysis of the varying charge states of λ-MnO_2 upon lithium incorporation predicts two equilibrium potentials at ≈3.9 and 4.1 V versus Li^+/Li, corresponding to the energy levels of two different intercalated Li^+ states with qualitatively distinct characters, in close agreement with the experimentally determined potentials. These results suggest that electronic charge switching, which is active in pseudocapacitive materials, may also be operative in other common battery materials. Furthermore, the success of the UEB framework in describing charge storage in $LiMn_2O_4$ suggests that the UEB framework can be used broadly to intelligently design new electrode materials for advanced batteries as well as other electrochemical systems.

By varying CV sweep rates between 1 and 400 mV s^{-1} to analyze the charge-storage character of ultrathin films of $LiMn_2O_4$ with variable thicknesses, we isolated the fraction of the charge-storage in $LiMn_2O_4$ that arises from nonsurface capacitive processes. We suggest that this fraction of the capacity, corresponding to 20%–30% of the total capacity, arises from electronic charge-switching of bulk $LiMn_2O_4$ that does not involve transport of a compensating amount of Li^+ in agreement with our theoretical calculations. Such electronic processes should proceed rapidly relative to ion transport, because they require no heavy-atom rearrangement. We propose that the development of new materials that exploit and optimize this effect could provide a new avenue for rapid and reversible charge-storage.

We also evaluate the ability of $LiMn_2O_4$ to store charge in electrolytes containing Na^+, K^+, and Mg^{2+}. We note small differences between the charge-storage behavior in electrolytes containing each of these cations corresponding to their relative size and charge. Notably, electrochemical redox peaks are observed in the range of 3.8–4.2 V for Li^+, Na^+, and K^+, but not for Mg^{2+}. We predict that Mg^{2+} may induce electrochemical redox peaks at potentials >1.1 V versus Ag/AgCl, however we were not able to measure the presence of these peaks due to the oxidative decomposition of water at potentials >1.1 V. The UEB framework enables a qualitative interpretation of how the type of intercalating ion will affect the expected equilibrium potential(s) for a given host material, which can be leveraged to predict the behavior of known cation intercalation electrode materials (e.g., lithium ion battery cathode materials) with new intercalating cations of emerging importance.

In summary, the novel synthesis of $LiMn_2O_4$, the fundamental understanding of charge storage in battery materials obtained from the unified electrochemical band diagram framework, and the observation of direct evidence for an electronic charge-switching storage mechanism described in this work have far-reaching implications for informing the development of future high-performance cathode materials for batteries based on cation-intercalation charge storage.

4. Methods Section

Electrochemical Conversion and Evaluation: Electrochemical conversion and analysis of the ALD-grown MnO films were performed with a two-channel SP-300 Potentiostat (BioLogic). A custom three-electrode flats evaluation cell was used to electrochemically characterize the manganese oxide films on stainless steel substrates. This custom electrochemical cell employed an

O-ring seal on the top surface of the sample, which exposed 1.21 cm^2 of the top surface coated by the MnO ALD film to the electrolyte.

A 0.10 M lithium sulfate (Alfa Aesar, 99.99% metals basis) aqueous electrolyte was used, where the pH was buffered to between 9 and 11 using lithium carbonate (Alfa Aesar, 99%). For each sample, fresh electrolyte was added to the cell, and for 10 min prior to and during electrochemical conversion/evaluation, the cell was purged with argon (Airgas, Prepurified). For the three-electrode measurements performed in this work, a platinum counter electrode and saturated Ag/AgCl reference electrode (BASi) were used.

For each sample, a two-step process was repeated to convert MnO to $LiMn_2O_4$. First, three CV loops were executed between –0.3 and 1.1 V versus a saturated Ag/AgCl reference electrode at a sweep rate (ν) of 10 mV s^{-1}. Then, a constant-potential oxidation was performed at a potential between 0.8 and 1.0 V. These two steps were repeated until the measured CV reached reversible steady-state behavior. Following conversion to $LiMn_2O_4$, additional CV experiments were performed at sweep rates of $1 \leq \nu \leq 400$ mV s^{-1} to evaluate the timescales of the processes contributing to charge storage.

Quantum Mechanical Calculations: The approach employed to calculate equilibrium potentials in $LiMn_2O_4$ expanded upon existing theoretical techniques that are limited to calculation of average insertion potentials.[25,26] Here, a method based on defect formation energy calculations[50–52] was used to calculate equilibrium potentials for charge storage in $LiMn_2O_4$ by determining the electronic energy levels at which electronic charge-switching becomes spontaneous.[24] Rather than relying on the intercalating ion elemental reference (e.g., metallic lithium for the Li^+/Li redox couple), the work function and band gap of the host material were employed to evaluate the equilibrium potentials for charge storage on an absolute scale. Although a rigid band model[25] was used to determine the absolute reference, total energy calculations of the lithiated λ-MnO_2 at varying charge states referenced to the host λ-MnO_2 were also used to explicitly describe the effects of ionic and electronic insertion on the band structure and determine the potentials at which charge-switching becomes favorable. This method provides a description which is more transferable to other electrode/electrolyte systems, including those where the ionic and electronic insertion processes are highly decoupled or where a suitable reference potential for the intercalating ion is not available.

For these calculations, the HSE06 with 25% exact exchange was used, which had been shown to accurately describe the electronic structure of various crystalline phases of MnO_2[24,53] and to accurately predict defect levels.[54] In order to model the electronic structure in a manner consistent with experimental operating temperatures and with the experimental observation of a Néel temperature well below 100 K for spinel $LiMn_2O_4$,[55] a constraint of low total spin was imposed by restricting calculations to spin configurations with low net spin. See Section 1 in the Supporting Information for further details of these calculations. The chemical potentials of all atomic species used for calculation of formation energies were determined based on the activity of a proton at a pH of 10, which was the approximate pH used in the electrochemical measurements in this work (see the Supporting Information of ref. [24] for details of the chemical potential derivation). Additionally, reported formation energiers were referenced to uncharged $LiMn_2O_4$. Note that the method of using the electrostatic potential to properly align the band structures between calculations and place them on an absolute scale rendered the calculated redox potentials insensitive to the chemical potentials of the atomic species used for evaluating the formation energies. Furthermore, shifts in the band edges caused by band bending in response to the double-layer field at the electrode–electrolyte interface were corrected. This was accomplished by using the point of zero charge (pH_{PZC}) and by assuming Nernstian behavior in the correction $\Delta E = -0.059(\mathrm{pH}\ \mathrm{pH}_{PZC})$ V. The pH_{PZC} of $LiMn_2O_4$ was taken to be 2, based on experimental results showing a $pH_{PZC} < 2.5$ for $LiMn_2O_4$.[56]

Supporting Information

Supporting Information is available from the Wiley Online Library or from the author.

Acknowledgements

This work was supported in part (M.J.Y.) by the National Science Foundation Graduate Research Fellowship under Grant No. DGE 1144083. C.B.M. acknowledges support from the NSF through grants CHE-1214131 and CBET-1433521. This work utilized the Janus supercomputer, which was supported by the National Science Foundation through CNS-0821794 and the University of Colorado Boulder. A.M.H. acknowledges support from the Center for Next Generation Materials by Design, an Energy Frontier Research Center funded by the U.S. Department of Energy, Office of Science, Basic Energy Sciences under Contract No. DE-AC36-08GO28308. Any opinion, findings, and conclusions or recommendations expressed in this material were those of the author(s) and did not necessarily reflect the views of the NSF.

Received: June 5, 2016
Revised: July 30, 2016
Published online: September 22, 2016

[1] V. Etacheri, R. Marom, R. Elazari, G. Salitra, D. Aurbach, *Energy Environ. Sci.* **2011**, *4*, 3243.
[2] M. Pasta, A. Battistel, F. La Mantia, *Energy Environ. Sci.* **2012**, *5*, 9487.
[3] J. Lee, S.-H. Yu, C. Kim, Y.-E. Sung, J. Yoon, *Phys. Chem. Chem. Phys.* **2013**, *15*, 7690.
[4] J. F. Whitacre, T. Wiley, S. Shanbhag, Y. Wenzhuo, A. Mohamed, S. E. Chun, E. Weber, D. Blackwood, E. Lynch-Bell, J. Gulakowski, C. Smith, D. Humphreys, *J. Power Sources* **2012**, *213*, 255.
[5] T. Ohzuku, M. Kitagawa, T. Hirai, *J. Electrochem. Soc.* **1989**, *136*, 3169.
[6] M. Nishizawa, T. Uchiyama, T. Itoh, T. Abe, I. Uchida, *Langmuir* **1999**, 4949.
[7] M. Thackeray, C. T. Division, E. T. Program, *Science* **1997**, *25*, 3.
[8] W. Tang, X. J. Wang, Y. Y. Hou, L. L. Li, H. Sun, Y. S. Zhu, Y. Bai, Y. P. Wu, K. Zhu, T. Van Ree, *J. Power Sources* **2012**, *198*, 308.
[9] M. B. Sassin, S. G. Greenbaum, P. E. Stallworth, A. N. Mansour, B. P. Hahn, K. A. Pettigrew, D. R. Rolison, J. W. Long, *J. Mater. Chem. A* **2013**, *1*, 2431.
[10] D. Guyomard, J. M. Tarascon, *J. Electrochem. Soc.* **1993**, *140*, 3071.

[11] M. Okubo, Y. Mizuno, H. Yamada, J. Kim, E. Hosono, H. Zhou, T. Kudo, I. Honma, *ACS Nano* **2010**, *4*, 741.
[12] B. Put, P. M. Vereecken, N. Labyedh, A. Sepulveda, C. Huyghebaert, I. P. Radu, A. Stesmans, *ACS Appl. Mater. Interfaces* **2015**, *7*, 22413.
[13] B. B. Burton, F. H. Fabreguette, S. M. George, *Thin Solid Films* **2009**, *517*, 5658.
[14] M. J. Young, M. Neuber, A. C. Cavanagh, H. Sun, C. B. Musgrave, S. M. George, *J. Electrochem. Soc.* **2015**, *162*, A2753.
[15] L. C. Ferracin, A. Amaral, N. Bocchi, *Solid State Ionics* **2000**, *130*, 215.
[16] K. Huang, B. Peng, *Sol. Energy Mater. Sol. Cells* **2000**, *62*, 177.
[17] C. Wan, Y. Nuli, J. Zhuang, Z. Jiang, *Mater. Lett.* **2002**, *56*, 357.
[18] M. Helan, L. J. Berchmans, *Mater. Manuf. Processes* **2011**, *26*, 1369.
[19] X. Wang, X. Chen, L. Gao, H. Zheng, M. Ji, T. Shen, Z. Zhang, *J. Cryst. Growth* **2003**, *256*, 123.
[20] H. Yue, X. Huang, D. Lv, Y. Yang, *Electrochim. Acta* **2009**, *54*, 5363.
[21] O. Nilsen, H. Fjellvåg, A. Kjekshus, *Thin Solid Films* **2003**, *444*, 44.
[22] O. Nilsen, S. Foss, H. Fjellvåg, A. Kjekshus, *Thin Solid Films* **2004**, *468*, 65.
[23] V. Miikkulainen, A. Ruud, E. Østreng, O. Nilsen, M. Laitinen, T. Sajavaara, H. Fjellvåg, *J. Phys. Chem. C* **2014**, *118*, 1258.
[24] M. J. Young, A. M. Holder, S. M. George, C. B. Musgrave, *Chem. Mater.* **2015**, *27*, 1172.
[25] Y. S. Meng, M. E. Arroyo-de Dompablo, *Energy Environ. Sci.* **2009**, *2*, 589.
[26] J. M. Chem, G. Hautier, A. Jain, H. Chen, C. Moore, S. P. Ong, G. Ceder, *J. Mater. Chem.* **2011**, *21*, 17147.
[27] J. D. Strenger-Smith, J. A. Irvin, *Mater. Matters* **2009**, *4.4*, 87.
[28] CoorsTek Specialty Chemicals, Products: Safety and Product Data Sheets.
[29] J. W. Fergus, *J. Power Sources* **2010**, *195*, 4554.
[30] W. H. Meyer, *Adv. Mater.* **1998**, *10*, 439.
[31] J. W. Fergus, *J. Power Sources* **2010**, *195*, 4554.
[32] A. Karim, S. Fosse, K. Persson, *Phys. Rev. B* **2013**, *87*, 075322.
[33] C. Fall, N. Binggeli, A. Baldereschi, *J. Phys.: Condens. Matter* **1999**, *2689*, 2690.
[34] J. Song, B. L. Hong, J. Zheng, P. Lin, M. Sen Zheng, Q. H. Wu, Q. F. Dong, S. G. Sun, *Appl. Phys. A: Mater. Sci. Process.* **2010**, *98*, 455.
[35] B. Ammundsen, P. B. Aitchison, G. R. Burns, D. J. Jones, J. Rozière, *Solid State Ionics* **1997**, *97*, 269.
[36] S. Fritsch, A. Navrotsky, *J. Am. Ceram. Soc.* **1996**, *79*, 1761.
[37] E. R. Stobbe, B. A. De Boer, J. W. Geus, *Catal. Today* **1999**, *47*, 161.
[38] B. Yin, S. Zhang, H. Jiang, F. Qu, X. Wu, *J. Mater. Chem. A* **2015**, *3*, 5722.
[39] M. E. Orazem, B. Tribollet, *Electrochemical Impedance Spectroscopy*, John Wiley & Sons, Hoboken, NJ **2008**.
[40] J. Wang, J. Polleux, J. Lim, B. Dunn, *J. Phys. Chem. C* **2007**, *111*, 14925.
[41] S. Ardizzone, G. Fregonara, S. Trasatti, *Electrochim. Acta* **1990**, *35*, 263.
[42] T. Brousse, M. Toupin, R. Dugas, L. Athouël, O. Crosnier, D. Bélanger, *J. Electrochem. Soc.* **2006**, *153*, A2171.
[43] P. Taylor, *Crystallographic Databases*, Vol. *44*, (Eds: F. H. Allen, G. Bergerhoff, R. Sievers), International Union of Crystallography, Chester, England **1987**, p. 221.
[44] R. Gummow, A. Dekock, M. Thackeray, *Solid State Ionics* **1994**, *69*, 59.
[45] M. Toupin, T. Brousse, D. Bélanger, *Chem. Mater.* **2004**, *16*, 3184.
[46] R. Benedek, M. M. Thackeray, A. van de Walle, *J. Mater. Chem.* **2010**, *20*, 369.
[47] E. B. Godunov, I. V. Artamonova, I. G. Gorichev, Y. A. Lainer, *Russ. Metall.* **2012**, *2012*, 935.
[48] *CRC Handbook of Chemistry and Physics*, 96th ed. (Eds: W. M. Haynes, D. R. Lide, T. J. Bruno), CRC Press/Taylor and Francis, Boca Raton, FL **2015**.
[49] Y. Marcus, *J. Chem. Soc., Faraday Trans.* **1991**, *87*, 2995.
[50] S. B. Zhang, J. E. Northrup, *Phys. Rev. Lett.* **1991**, *67*, 2339.
[51] C. G. Van de Walle, *J. Appl. Phys.* **2004**, *95*, 3851.
[52] A. M. Holder, K. D. Osborn, C. J. Lobb, C. B. Musgrave, *Phys. Rev. Lett.* **2013**, *111*, 065901.
[53] C. Franchini, R. Podloucky, J. Paier, M. Marsman, G. Kresse, *Phys. Rev. B* **2007**, *75*, 1.
[54] P. Deák, B. Aradi, T. Frauenheim, E. Janzén, A. Gali, *Phys. Rev. B: Condens. Matter Mater. Phys.* **2010**, *81*, 1.
[55] I. Tomeno, Y. Kasuya, Y. Tsunoda, *Phys. Rev. B* **2001**, *64*, 1.
[56] M. Kosmulski, *Surface Charging and Points of Zero Charge*, CRC Press, Boca Raton, FL **2010**.
[57] F. Izumi, *Solid State Ionics* **2004**, *172*, 1.
[58] K. Momma, F. Izumi, *J. Appl. Crystallogr.* **2011**, *44*, 1272.
[59] A. Jain, S. P. Ong, G. Hautier, W. Chen, W. D. Richards, S. Dacek, S. Cholia, D. Gunter, D. Skinner, G. Ceder, K. A. Persson, *APL Mater.* **2013**, *1*, 011002.